PAPER

Regulating phase change behavior and surface characteristics of Sn$_{15}$Sb$_{85}$ thin film by oxygen doping

View the article online for updates and enhancements.

IOP ebooks™

Bringing you innovative digital publishing with leading voices to create your essential collection of books in STEM research.

Start exploring the collection - download the first chapter of every title for free.

Regulating phase change behavior and surface characteristics of $Sn_{15}Sb_{85}$ thin film by oxygen doping

Yifeng Hu[1,3,4,5], **Haipeng You**[1]**, Qingqian Chou**[2] **and Tianshu Lai**[2,5]

[1] School of Mathematics and Physics, Jiangsu University of Technology, Changzhou 213000, People's Republic of China
[2] State-Key Laboratory of Optoelectronic Films and Technology, School of Physics, Sun Yat-Sen University, Guangzhou 510275, People's Republic of China
[3] State Key Lab of Silicon Materials, Zhejiang University, Hangzhou 310027, People's Republic of China
[4] Key Laboratory of Microelectronic Devices and Integrated Technology, Institute of Microelectronics, Chinese Academy of Sciences, Beijing 100029, People's Republic of China

E-mail: hyf@jsut.edu.cn (Y Hu) and stslts@mail.sysu.edu.cn (T Lai)

CrossMark

Abstract

In this paper, oxygen doped $Sn_{15}Sb_{85}$ thin films were proposed to reduce the power consumption for phase change memory (PCM) application. Compared with $Sn_{15}Sb_{85}$, oxygen doped $Sn_{15}Sb_{85}$ thin film had higher crystallization temperature (168 °C–255 °C) and broader energy band gap (1.23–1.55 eV). X-ray diffraction patterns and transmission electron microscope showed that the crystallization of thin film was suppressed and grains became smaller when oxygen was added. After oxygen doping, the surface roughness decreased from 13.6 to 2.5 nm. Antimony oxide formed to enhance the thermal stability. In comparison to $Ge_2Sb_2Te_5$, oxygen doped $Sn_{15}Sb_{85}$ had an ultra-fast phase transition speed (3.9 ns) confirmed by laser picosecond technology. The result of differential scanning calorimetry revealed that oxygen doped $Sn_{15}Sb_{85}$ had a lower melting temperature (494 °C). PCM cells based on the oxygen doped $Sn_{15}Sb_{85}$ thin film were fabricated to evaluate the electrical characteristics as well. The results indicated that the oxygen doped $Sn_{15}Sb_{85}$ thin film had great potentiality in PCM application.

Keywords: oxygen doping, power consumption, thermal stability, surface characteristic

(Some figures may appear in colour only in the online journal)

1. Introduction

Among the potential semiconductor memories, phase change memory (PCM) has many merits to make it the most promising technology for next generation of non-volatile memory, such as ultra-fast speed, high density, long fatigue life and compatible with the complementary metal oxide semiconductor (CMOS) technology [1, 2]. The mechanism for data storage is based on the reversible phase change of a chalcogenide alloy between the unordered insulating structure and ordered conductive one induced by the pulse current or laser. In order to meet the requirement in embedded memory application, the two major problems should be solved. One is that the floating body effect becomes more and more serious with the continuous reduction of device size, which results in the thermal crosstalk between adjacent device cells [3]. The better amorphous thermal stability of phase change materials should be achieved to have good data retention. Besides, the switching speed between different resistance values should be improved to move forward a single step to compete with NOR-flash memory [4].

Te-based chalcogenide film is currently the most widely used phase change material in PCM, such as Ge–Sb–Te and Sb–Te series [5, 6]. However, Te atoms in the thin film easily

[5] Authors to whom any correspondence should be addressed.

1

J. Phys. D: Appl. Phys. **52** (2019) 415104

Y Hu *et al*

separate from phase change film at higher temperature [7, 8]. This phase separation may decrease the repeatability of the phase transition and shorten the cycle life of the device [9, 10]. Therefore, Te-free phase change materials may have better prospects in PCM application. In literatures, Sb-rich and Te-free phase change materials have been proved with a high crystallization velocity and good archives stability in phase change optical storage [11, 12]. Recently, these phase change materials are also applied to electric phase change storage. In a previous work of ours, Sb-rich $Sn_{15}Sb_{85}$ film has been demonstrated to possess fast crystallization rate due to its growth dominated crystallization mechanism [13]. Moreover, the low melting point of Sn helps to reduce the power consumption in RESET operation. Therefore, Sn has been used as a doping agent to optimize the phase change materials [14, 15]. The downside for $Sn_{15}Sb_{85}$ is its poor thermal stability [16, 17]. Therefore, the stability of $Sn_{15}Sb_{85}$ needs to be improved by means of doping or compositing. Oxygen is a common dopant because the method is simple and effective, which has been put into effect for Sb–Te [18, 19], Ge–Sb–Te [20, 21] and Si–Sb [22]. The right amount of doped oxygen can improve the thermal stability [23], but excess oxygen is prejudicial [24]. In this work, the O-doped $Sn_{15}Sb_{85}$ thin films with different oxygen content were prepared and the influence of oxygen was investigated in details by adopting electrical, optical and thermal methods.

2. Experimental methods

$Sn_{15}Sb_{85}$, $Ge_2Sb_2Te_5$ and O-doped $Sn_{15}Sb_{85}$ thin films with the thickness of 100 nm were deposited on the 0.5 mm thick silicon dioxide (1 0 0) wafers by a radio-frequency (RF) magnetron sputtering system at room temperature. The oxygen content was determined by controlling the ratio of argon to oxygen while the total gas flow was fixed at 30 sccm in the whole sputtering process. The atomic percent content of oxygen element was determined by x-ray photoelectron spectroscopy (XPS) (shown in table 1). The SS and SSOX (X is oxygen flow) represent undoped and O-doped $Sn_{15}Sb_{85}$ thin films. The background pressure and sputtering pressure were 3.5×10^{-4} and 4×10^{-1} pa, respectively. The purity of $Sn_{15}Sb_{85}$ target was 99.999 at.%. The sputtering power of $Sn_{15}Sb_{85}$ target was 35 W. The sample plates with silicon wafer were kept rotating 20 rmp to guarantee the homogeneity of deposited thin films in the vacuum chamber.

The resistance as a function of temperature (*R–T*) was measured using the *in situ* measurement with a heating rate of 10 °C min^{-1}. The sample temperature was measured by a Pt-100 thermocouple located at a heating stage controlled by a TP 94 temperature controller (Linkam Scientific Instruments Ltd, Surrey, UK). The optical band gap was measured by NIR spectrophotometer. The phase structures of the films annealed at various temperatures were investigated by x-ray diffraction (XRD) analysis using Cu *Ka* radiation in the 2*θ* range from 20° to 60°, with a scanning step of 0.01°. The atomic force microscopy (AFM, FM-Nanoview 1000) was used to examine the surface topography. The chemical composition and chemical

Table 1. The technological parameter for sputtering.

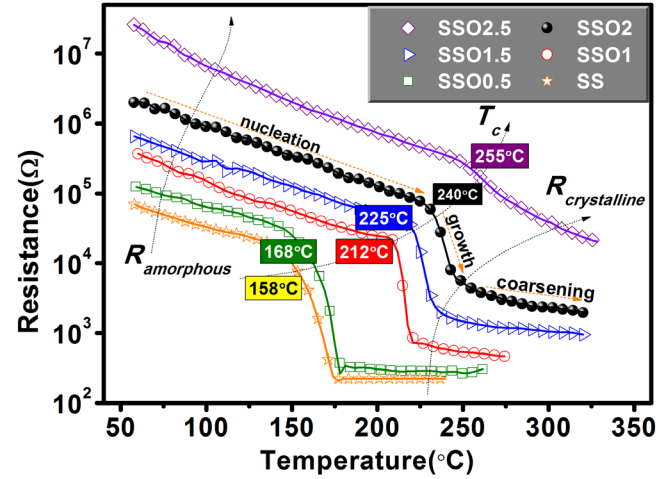| Sample symbol	Flow rate of O_2 (sccm)	Flow rate of Ar (sccm)	Oxygen content (at.%)
SS	0.0	30.0	0.0
SSO0.5	0.5	29.5	1.9
SSO1	1.0	29.0	3.6
SSO1.5	1.5	28.5	6.2
SSO2	2.0	28.0	7.5
SSO2.5	2.5	27.5	9.3

Figure 1. The electrical resistance as functions of temperature of SS and SSOX (*x* = 0.5, 1, 1.5, 2 and 2.5) thin films with a heating rate of 10 °C min^{-1}.

bonding state of elements in the SSOX thin films were determined by means of XPS analysis. A picosecond laser pump-probe system was used for real-time reflectivity measurement. The light source used for irradiating the samples was a frequency-doubled and model-locked neodymium yttrium aluminum garnet laser operating at 532 nm wave-length with a pulse duration of 30 ps. The melting point temperature (T_m) was detected via differential scanning calorimetry (DSC). The microstructure analysis was carried out using transmission electron microscopy (TEM) (JEOL 2010) and the samples with 100 nm thickness were fabricated on the copper mesh with a carbon film. The device properties of PCM cell were measured using a Tektronix AWG5012B arbitrary waveform generator and a Keithley 2602A parameter analyzer.

3. Results and discussions

Figure 1 shows *R–T* curves of SS and SSOX thin films at the heating rate of 10 °C min^{-1}. With the increase of temperature, a continuous reduction in amorphous resistance is observed for all thin films, which is explained by the thermally activated hopping transport mechanism [25]. Before crystallization, the amorphous resistances increase from 5.02×10^4 Ω of SS to 1.49×10^7 Ω of SSO2.5 thin film in table 2. Similarly, the increasing of crystalline resistance also exceeds two orders of magnitude after O-doping. According to the joule heat equation $Q = I^2 \cdot R \cdot t$, a larger resistance can enhance the heating efficiency, resulting in a lower power consumption for both

J. Phys. D: Appl. Phys. **52** (2019) 415104

Y Hu *et al*

Table 2. Sectional phase-change characteristics for SS and SSOX thin films.

Thin films	Amorphous resistance (Ω)	Crystalline resistance (Ω)	Crystallization temperature (°C)	E_g (eV)
SS	5.02×10^4	2.03×10^2	158	1.19
SSO0.5	1.03×10^5	2.83×10^2	168	1.23
SSO1	2.87×10^5	6.57×10^2	212	1.28
SSO1.5	4.79×10^5	1.79×10^3	225	1.42
SSO2	1.47×10^6	5.09×10^3	240	1.55
SSO2.5	1.49×10^7	3.52×10^4	255	—

SET and RESET programming. Crystallization temperature (T_c) is a significant index for phase-change storage thin film to estimate its thermal stability [26]. In figure 1, with the increasing of oxygen content, the T_c of SSOX thin film rises synchronously, indicating a better thermal stability for PCM after O-doping. Meanwhile, there is a sufficient resistance difference over one order of magnitude between amorphous and crystalline state for SSOX ($x = 0.5, 1, 1.5$ and 2) thin films to ensure the enough signal to noise ratio (SNR). It is worth noting that the phase-change behavior becomes tardy and unconspicuous when the oxygen flow reaches 2.5 sccm. It reveals that too much oxygen can restrain the crystallization and have a negative impact on PCM.

As shown in figure 2, the band gap energy E_g of amorphous films is determined by extrapolating the absorption edge onto the energy axis. The conversion of reflectivity to absorbance data is gained according to Kubelka–Munk function (K–M) [27]:

$$K/S = (1 - R)^2 / (2R), \qquad (1)$$

where K, S and R are the reflectivity, scattering coefficient and absorption coefficient, respectively.

Figure 2 shows the plots of absorbance versus energy for amorphous SS and SSOX films. By extrapolating the linear portion of curves to zero absorption, the E_g are determined to be SS ~ 1.19, SSO0.5 ~ 1.23, SSO1 ~ 1.28, SSO1.5 ~ 1.42 and SSO2 ~ 1.55 eV, respectively. Obviously, E_g is enhanced with the increase of oxygen content, which may be caused by the increase of the randomness of the atomic configuration of the thin film. The increase of disorder leads to the transition from the delocalized electron state to the localized electron state, resulting in the enhancement of electron scattering and the decrease of electrical conductivity [28]. In general, a larger E_g is beneficial to reduce the threshold current of PCM.

XRD patterns of SS, SSO1.5 and SSO2 thin films annealed at different annealing temperature are shown in figure 3. No obvious diffraction peaks are observed for three kinds of as-deposited thin films except for a gentle peak at 28.6°. When the annealing temperature reaches 170 °C, two diffraction peaks for SS thin film firstly appear belonging to SnSb (101) and Sb (110) phases (show in figure 3(a)). At 260 °C, the peaks become stronger and a new diffraction peak SnSb (021) emerges, indicating the more sufficient crystallization. The diffraction peaks SnSb (101) and (021) in SS thin film are identified as having rhombohedral structure (R-$3m$), which is known to be a representative A7 phase [29]. The lattice
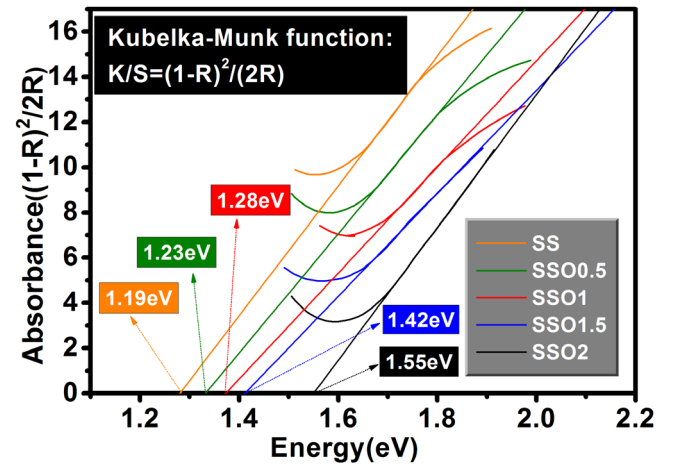
Figure 2. The Kubelka–Munk function of amorphous SS and SSOX ($x = 0.5, 1, 1.5$ and 2) thin films.

parameters of SnSb crystals are measured to $a = 4.28$ Å and $c = 11.36$ Å. For SSO1.5 thin film (figure 3(b)), the analogous crystallization process is observed. However, the first diffraction peak appears till the temperature 280 °C and the intensity of peaks weakens. Figure 3(c)) displays the crystallization process for SSO2 thin film. Only a blurred diffraction peak SnSb (101) is observed after annealing at 300 °C. By comparing the above results, it suggests that crystallization process of SSO1.5 and SSO2 thin films are inhibited with the addition of oxygen atoms. From the main peak at around 28.6°, the grain size of annealed SS, SSO1.5 and SSO2 thin films are 28.6, 18.5 and 15.3 nm, respectively, calculated using the Scherrer equation, assuming no stress effect [30]:

$$D_{hkt} = 0.943\lambda / (\beta \cos \theta) \qquad (2)$$

where λ is wavelength of the x-ray, β is the full-width-at-half-maximum (FWHM), and θ is the diffraction angle. It can be concluded that the oxides may exist in amorphous state around the SnSb grains, serving as centers for suppression of the grains' growth. As a result, the crystallization becomes more difficult and the thermal stability of the amorphous state improves. Besides, the smaller grain size will generate more grain boundaries, which can enhance electron scattering and reduce the free carriers [31].

In phase transition, the change of inner structure will cause the variation of surface topography and stress redistribution. Film surface roughness has a significant impact on device reliability because the induced stress can affect the quality of the electrode-film interface during the phase change process
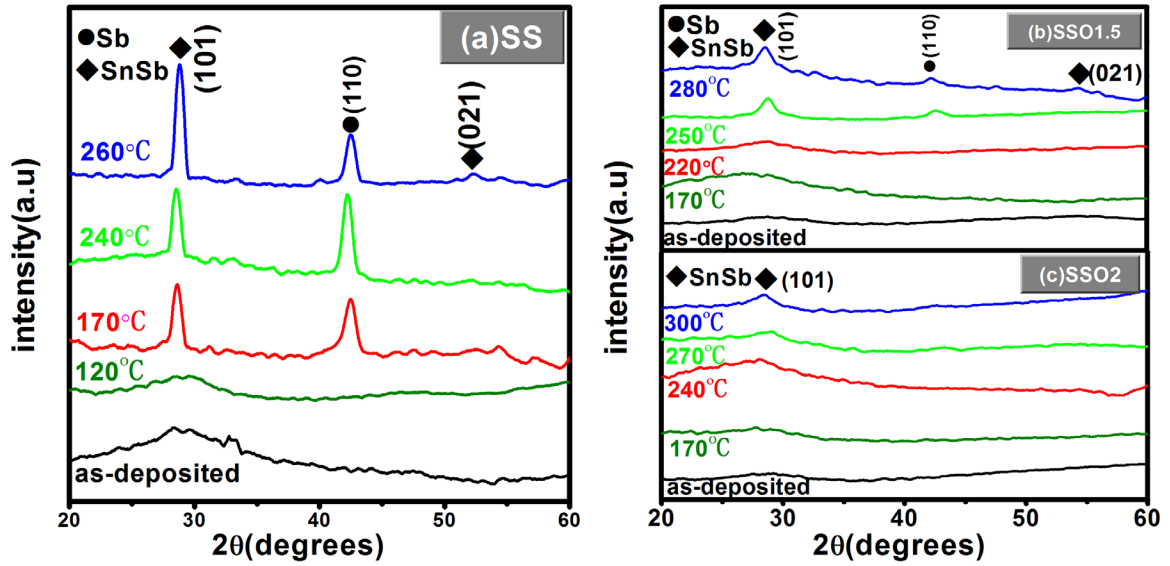
J. Phys. D: Appl. Phys. **52** (2019) 415104

Y Hu *et al*

Figure 3. XRD patterns of (a) SS, (b) SSO1.5 and (c) SSO2 thin films annealed at different annealing temperature.
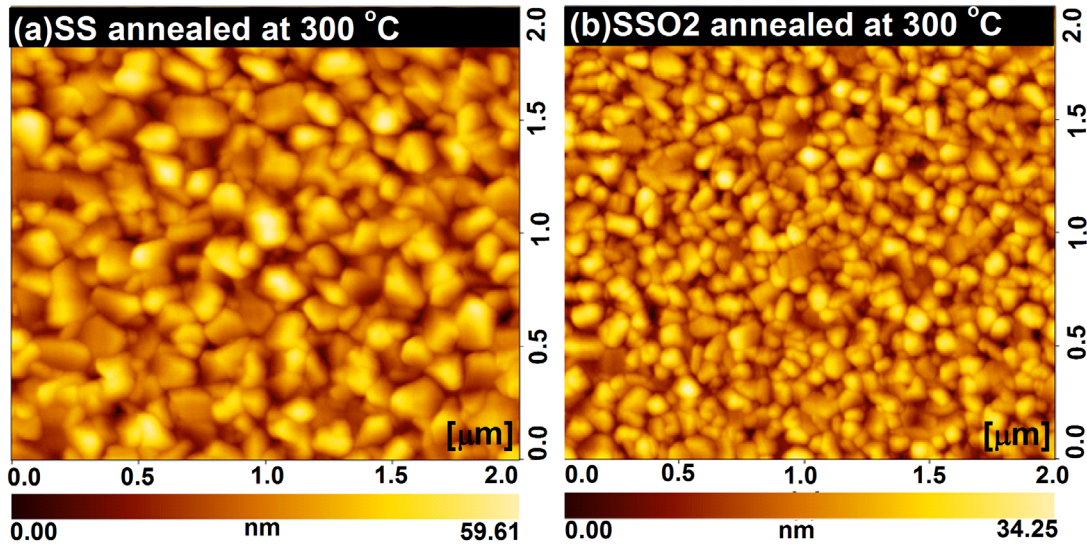

Figure 4. AFM topographic images of (a) SS and (b) SSO2 thin films annealed at 300 °C for 20 min.

[32]. The AFM topographic images of SS and SSO2 thin films annealed at 300 °C for 20 min are presented in figure 4. A mass of grains can be observed in both annealed SS and SSO2 thin films. Compared with SS, SSO2 is more uniform in size and compact in structure. The quantitative result of root-mean-square (RMS) roughness shows that SSO2 thin film have smaller RMS (2.5 nm) than SS (13.6 nm). The reduction of RMS value indicates a better contact between top electrode and phase-change thin film and it is beneficial for the fatigue performance of PCM.

In PCM devices, the power consumption of the whole phase-change process is mainly determined by the energy required in the RESET process, because the SET process requires less energy and longer time while the RESET one needs a sharp cooling or a strong pulse to cause its inverse phase change. The inset in figure 5 shows the reflectivity evolutions in the amorphization process (RESET) for SS, SSO2 and $Ge_2Sb_2Te_5$ thin films. All thin films have a sudden drop in
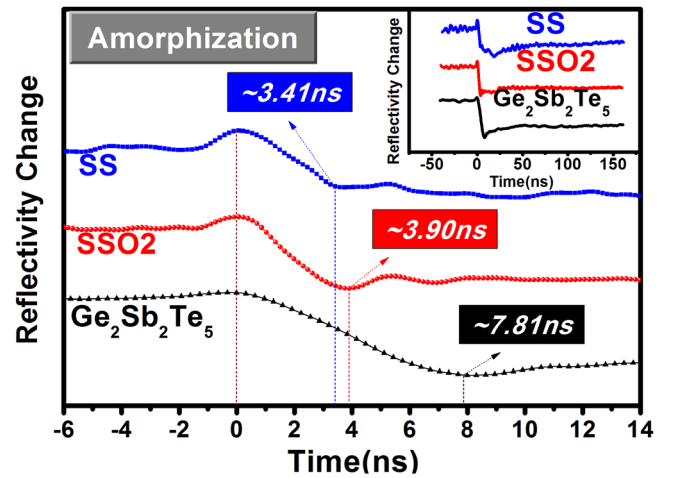

Figure 5. The enlarged figure of reflectivity evolutions in the amorphization process for SS, SSO2 and $Ge_2Sb_2Te_5$ thin films. Inset shows the original curves with full time horizon.

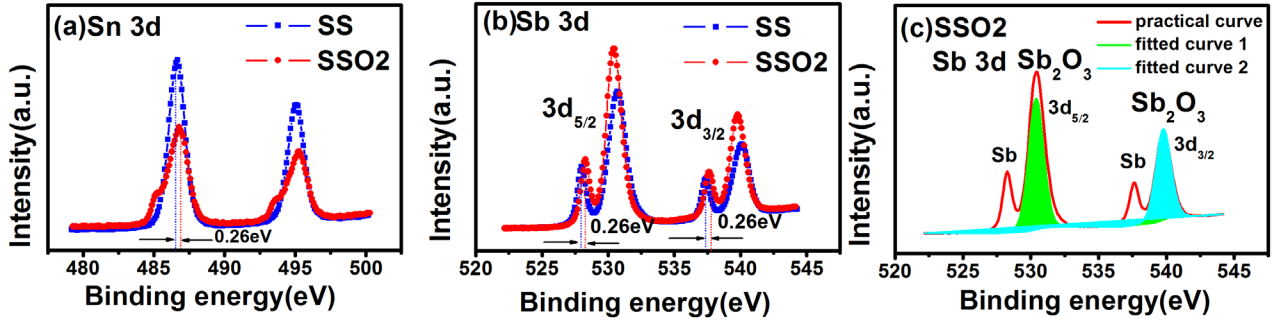J. Phys. D: Appl. Phys. **52** (2019) 415104

Y Hu *et al*

Figure 6. XPS spectra of (a) Sn 3*d* and (b) Sb 3*d* for SS and SSO2 thin films annealed at 300 °C for 3 min, respectively. (c) Fitted curves of Sb 3*d* for crystalline SSO2 thin film.

reflectivity under the same laser irradiation intensity of 20 mJ cm^{-2}, corresponding to the crystalline-to-amorphous transition. In order to compare the switching time, the detail with enlarged scale is provided. The amorphization time for SS and SSO2 is 3.41 and 3.90 ns, respectively. In spite of a slight increase in phase change time comparing to SS, SSO2 has a much faster switching velocity than $Ge_2Sb_2Te_5$ (7.81 ns). On the other hand, it confirms that SSO2 thin film has a lower operation power than $Ge_2Sb_2Te_5$ due to its shorter transform time. The previous literatures demonstrate that in Sb-rich phase change materials there are a great deal of Sb crystal nucleus, which provides many starting positions for crystallization and accelerates the phase change of the material [33].

XPS spectra of Sn 3*d* and Sb 3*d* belonging to SS and SSO2 thin films are shown in figure 6. As we can see in figure 6(a), the peak of Sn 3*d* homopolar bond (Sn–Sn) belonging to SS thin film is 486.80 eV, which is 0.26 eV smaller than SSO2 thin film. It also indicates that Sn atom has bonded with O atom. Previous literature reports that Sb $3d_{5/2}$ and Sb $3d_{3/2}$ peaks for the homopolar Sb (Sb–Sb) are detected at 527.6 eV and 536.9 eV, respectively, which is similar to the Sb peak in figure 6(b) [34]. In oxygen-doped SS, the location of peak for Sb $3d_{5/2}$ and Sb $3d_{3/2}$ moves towards higher binding energy area, which reveals that the Sb oxides have gradually formed. Figure 4(c) shows the fitted curves of Sb $3d_{5/2}$ and Sb $3d_{3/2}$ peaks of SSO2 thin film. The binding energy for Sb $3d_{5/2}$ and Sb $3d_{3/2}$ peaks is 528.2 eV and 537.6 eV, respectively. Compared the peak position of Sb to the database, these peaks correspond to the Sb–Sb bonds. The binding energy belonging to Sb–O bond configuration is 530.4 eV and 539.9 eV. It is known that the electronegativity of Sn, Sb and O elements are 1.96, 2.05 and 3.44, respectively, which signifies that O atom is much easier to bond with Sn and Sb atom to form the oxides. As a result, the thermal stability is improved. Besides, oxides are apt to condense near grain boundaries and wrap around the crystal grains, which will lead to produce smaller size grains and more grain boundaries.

Usually, the melting point temperature (T_m) is detected for phase-change thin film via conventional DSC [35]. Figure 7(a) shows DSC curve of SSO2 thin film at the heating rate of 5 °C min^{-1}. The inset in figure 7(a) shows the drawing of partial enlargement. Here, T_m of SSO2 thin film is 494 °C, which is much lower than that of traditional $Ge_2Sb_2Te_5$ (around 620 °C) [36]. The T_m is further confirmed by differentiation of
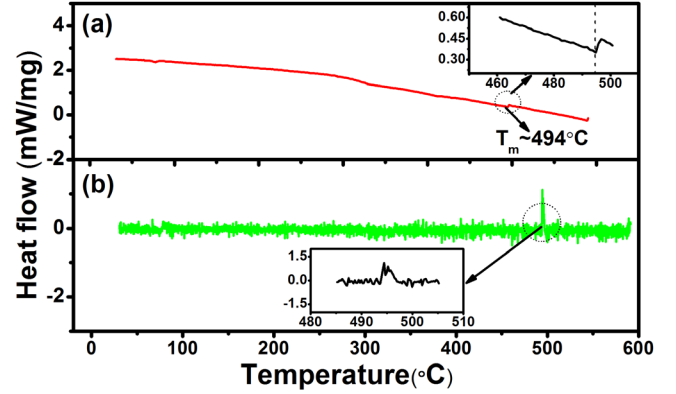

Figure 7. (a) DSC and (b) DDSC curves of SSO2 thin film at the heating rate of 5 °C min^{-1}. The insets are the drawings of partial enlargement.

DSC (DDSC) in figure 7(b) and the corresponding enlarged drawing. In RESET operation, the phase change material should be heated to above T_m. Therefore, a lower T_m can decrease the RESET power consumption during the whole phase transition process.

Figure 8 showed the bright-field (BF) TEM, high-resolution (HRTEM) and selected area electron diffraction (SAED) patterns of SS and SSO2 thin films annealed at 300 °C in an Ar atmosphere for 20 min. Figure 8(a) presents lots of crystallized regions arranged in an orderly manner. Figure 8(b) is an enlarged image of a local area ① in figure 8(a). A rhombohedral structure of Sb phase without extra phase was confirmed by identifying crystal plane orientation in figure 8(b) and the SAED of figure 8(c) [34]. In figure 8(d), the crystallization area in the SSO2 thin film is significantly reduced, which should be the result of the inhibition of oxides. HRTEM in figure 8(e) shows that the grains become denser and smaller in size. The SAED in figure 8(f) basically inherited the crystal plane orientation of figure 8(c). In addition, the diffraction spots in figure 8(f) are significantly less than that in figure 8(c), indicating that the crystallization is inhibited after oxygen doping. The smaller grains are helpful to improve the amorphous thermal stability and crystalline resistance of the film.

The PCM cells based on SS and SSO2 thin film were fabricated to test and verify the electrical properties using 0.18 μm CMOS technology with tungsten bottom electrode of 260 nm
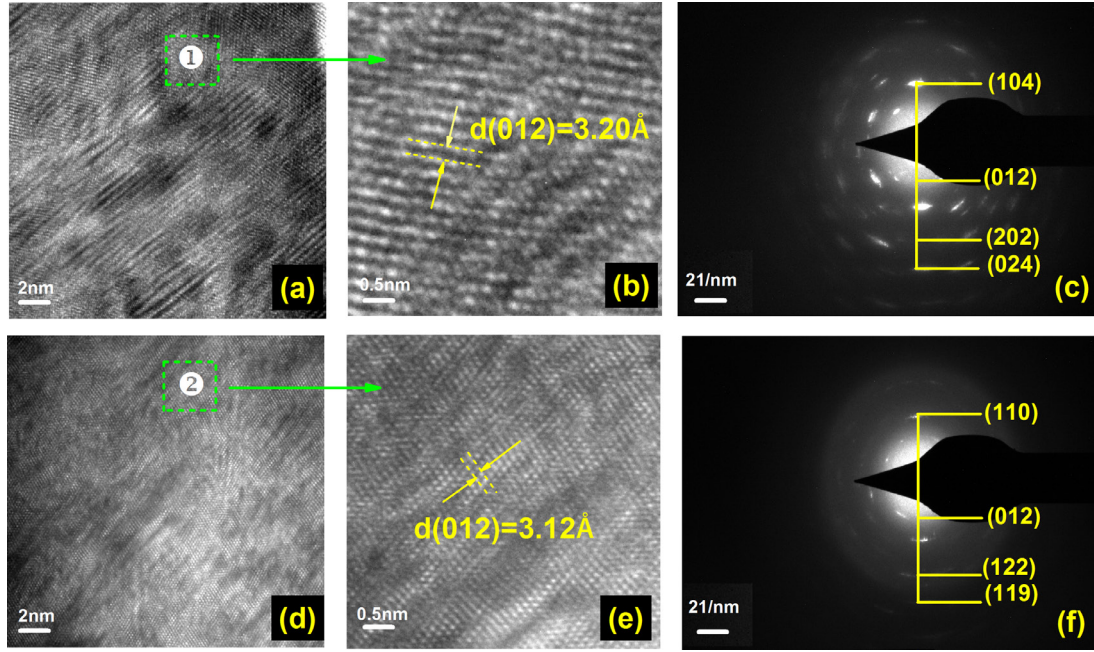
J. Phys. D: Appl. Phys. **52** (2019) 415104

Y Hu *et al*

Figure 8. The TEM BF images with corresponding HRTEM and SAED patterns for SS (a)–(c) and SSO2 (d)–(f) thin films, respectively.
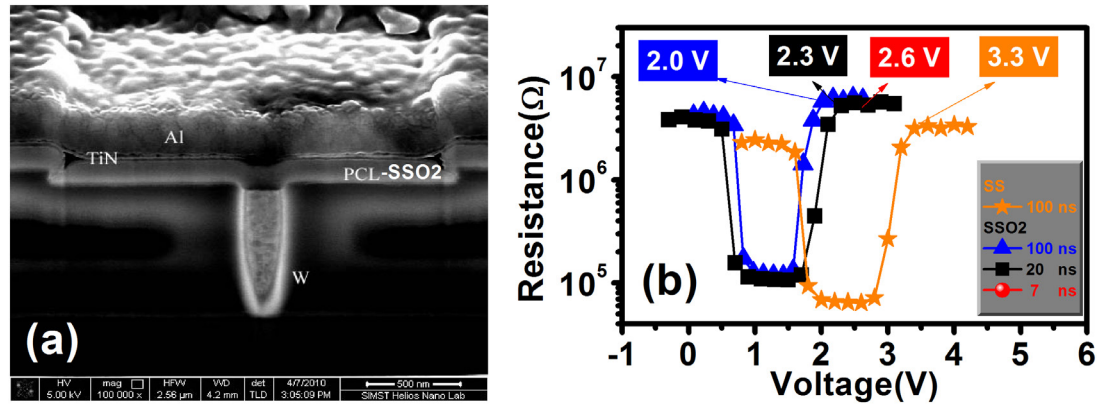

Figure 9. (a) The scanning electron microscopy image of PCM cell device; (b) *R*–*V* curves of SS and SSO2-based PCM devices.

in diameter. The scanning electron microscopy image of PCM cell device is shown in figure 9(a). A 20 nm-thick TiN layer is deposited so as to improve the interface between the phase change layer (PCL) and top electrode (Al). The thickness of phase change film was set at 100 nm. Figure 9(b) shows that the reversible resistance switching can be realized by the electrical pulse with different widths. The difference between high and low resistance state is close to two orders of magnitude, which is enough for PCM application. In addition, the threshold voltage of 2.6 V can be achieved by an electrical pulse with the width 7 ns. Compared with SSO2, $Ge_2Sb_2Te_5$-based PCM device is difficult to trigger the phase transition when the pulse width is shorter than 100 ns [35]. Induced by the same voltage pulse of 100 ns width, the RESET threshold voltage for SSO2 is 2.0 V, which is lower than SS (3.3 V) and $Ge_2Sb_2Te_5$ (3.6 V) films [37]. The necessary energy for RESET operation E_{reset} can be estimated by $\left(V_{reset}^2/R_{reset}\right) \times t_{reset}$. The energy for the RESET operation of SSO2 cell is calculated to be around 3.9×10^{-13} J,

which is approximately three orders of magnitude lower than that of $Ge_2Sb_2Te_5$ cell (9.7×10^{-10} J) [38].

4. Conclusions

In this work, oxygen doped $Sn_{15}Sb_{85}$ thin films were prepared by magnetron sputtering. After oxygen doping, the T_c increased from 158 °C of SS to 240 °C of SSO2 and 255 °C of SSO2.5. Except the monotone increasing of resistance with the oxygen content, the E_g was also broadened from 1.19 eV to 1.55 eV. The grains were refined with the size decreasing from 28.6 to 15.3 nm. The RMS surface roughness for SSO2 thin film was 2.5 nm, which was smaller than SS (13.6 nm). The formation of antimony oxides resulted in more small grains and grain boundaries. The existence of rich Sb elements and low melting temperature (494 °C) worked together to enable the SSO2 to have ultra-fast switching speed (3.9 ns for material and 7 ns for device) and low power consumption

J. Phys. D: Appl. Phys. **52** (2019) 415104

Y Hu *et al*

$(3.9 \times 10^{-13}$ J for RESET operation). In a word, oxygen doped $Sn_{15}Sb_{85}$ thin film was the promising candidate for high speed and low power for PCM application.

ORCID iDs

Yifeng Hu ⓘ https://orcid.org/0000-0001-7088-6829
Tianshu Lai ⓘ https://orcid.org/0000-0003-3978-583X

References

[1] Ielmini D and Lacaita A L 2011 *Mater. Today* **14** 600
[2] Caldwell M, Jeyasingh R, Wong H and Milliron D 2012 *Nanoscale* **4** 4382
[3] Zhang C, Song Z, Wu G, Liu B, Wan X, Wang L, Wang L, Yang Z, Chen B and Feng S 2011 *IEEE. Electr. Device* **32** 1014
[4] Loke D and Elliott S R 2012 *Science* **336** 1566
[5] Chen Y M, Mu S, Wang G X, Shen X, Wang J Q, Dai S X, Xu T F, Nie Q H and Wang R P 2017 *Appl. Phys. Express* **10** 105601
[6] Wang G X *et al* 2012 *J. Appl. Phys.* **111** 093514
[7] Zhang T, Song Z, Feng W, Bo L, Feng S and Bomy C 2007 *Appl. Phys. Lett.* **91** 221102
[8] Putero M, Coulet M V, Muller C, Baehtz C, Raoux S and Cheng H Y 2016 *Appl. Phys. Lett.* **108** 101909
[9] Lu Y G, Song S N, Gong Y F, Song Z T, Rao F, Wu L C, Liu B and Yao D N 2011 *Appl. Phys. Lett.* **99** 243111
[10] Li Z, Si C, Zhou J, Xu H B and Sun Z M 2016 *ACS Appl. Mater. Interfaces* **8** 26126
[11] Zhang T, Song Z, Liu B and Feng S 2008 *Semicond. Sci. Technol.* **23** 055010
[12] Chen Y M, Shen X, Wang G X, Xu T F, Wang R P, Dai S X and Nie Q H 2016 *J. Appl. Phys.* **120** 015301
[13] Rao F, Song Z T, Ren K, Li X L, Wu L C, Xi W and Liu B 2009 *Appl. Phys. Lett.* **95** 032105
[14] Lee M L, Yong K T, Gan C L, Ting L H, Muhamad Daud S B and Shi L P 2008 *J. Phys. D: Appl. Phys.* **41** 215402
[15] Singh G, Kaura A, Mukul M and Tripathi S K 2013 *J. Mater. Sci.* **48** 299
[16] He Z F, Wu P Z, Liu R R, Zhai J W, Lai T S, Song S N and Song Z T 2016 *Crystengcomm* **18** 1230
[17] Liu R R, Wu P Z, He Z F, Zhai J W, Liu X Y and Lai T S 2017 *Thin Solid Films* **625** 11
[18] You Y, Morioka S, Kozaki S, Satoh R and Hosaka S 2015 *Appl. Surf. Sci.* **349** 230
[19] Hu Y, Sun M, Song S, Song Z and Zhai J 2013 *J. Alloys Compd.* **551** 551
[20] Liu B, Song Z T, Zhang T, Feng S L and Chen B M 2005 *Appl. Surf. Sci.* **242** 62
[21] Yang T Y, Cho J Y, Park Y J and Joo Y C 2012 *Acta Mater.* **60** 2021
[22] Yin Z, Jie F and Bingchu C 2009 *Semicond. Sci. Technol.* **24** 045016
[23] Tae Hee J, Hun S, Kwang Lyul L, Sung Min C, Sang Jun K and Sang Youl K 2001 *Japan. J. Appl. Phys.* **40** 1609
[24] Liu B, Song Z and Feng S 2005 *Physics* **34** 279
[25] Hu Y F, Guo X, Chou Q Q and Lai T S 2018 *Chin. Phys. Lett.* **35** 096801
[26] Poffo C M, de Lima J C, Souza S M, Trichês D M, Borges Z V and de Biasi R S 2018 *J. Mater. Sci.* **53** 13451
[27] Yifeng H, Zhu X, Zou H, Zheng L, Song S and Song Z 2017 *J. Alloys Compd.* **696** 150
[28] Zhou X L, Wu L C, Song Z T, Rao F, Zhu M, Peng C, Yao D N, Song S N, Liu B and Feng S L 2012 *Appl. Phys. Lett.* **101** 142104
[29] Wuttig M, Bhaskaran H and Taubner T 2017 *Nat. Photon.* **11** 465
[30] Wu W H, Chen S, Zhai J, Liu X, Lai T, Song S and Song Z 2017 *Appl. Phys. Lett.* **110** 181906
[31] Wang Z R *et al* 2017 *Nat. Mater.* **16** 101
[32] Lu Q Y, Bishop S R, Lee D, Lee S, Bluhm H, Tuller H L, Lee H N and Yildiz B 2018 *Adv. Funct. Mater.* **28** 1803024
[33] Yifeng H, Li S, Lai T, Song S, Song Z and Zhai J 2013 *Scr. Mater.* **69** 61
[34] Wu W, He Z, Chen S, Zhai J, Song S and Song Z 2017 *J. Phys. D: Appl. Phys.* **50** 095602
[35] Chen C *et al* 2017 *Phys. Rev.* B **95** 09411
[36] Bin C, Van Lam D, Gertten B, George P, Petra R and Bart J K 2018 *Nanotechnology* **29** 505706
[37] Zhu X Q, Hu Y F, Zou H, Zhang J H, Sun Y M, Wu W H, Yuan L, Zhai L J, Song S N and Song Z T 2016 *Scr. Mater.* **66** 12166
[38] Matsubara E *et al* 2016 *Phys. Rev. Lett.* **117** 135501